

# Glucose transport via the Pseudomonads porin OprB. Implications for the design of Trojan-horse antinfectives.

Joan Coines,<sup>1</sup> Silvia Acosta-Gutierrez,<sup>2</sup> Igor Bodrenko<sup>2</sup>, Carme Rovira,<sup>1,3</sup> and Matteo Ceccarelli<sup>2,4\*</sup>.

[1] Departament de Química Inorgànica i Orgànica and Institut de Química Teòrica i Computacional (IQTUB), Universitat de Barcelona, Martí i Franquès 1, 08028 Barcelona, Spain. [2] Department of Physics, University of Cagliari, Cittadella Universitaria, S.P.8–km 0.700, 09042 Monserrato, Cagliari, Italy. [3] Institució Catalana de Recerca i Estudis Avançats (ICREA), Passeig Lluís Companys 23, 08018, Barcelona, Spain. [4] Istituto Officina dei Materiali (CNR - IOM) Cagliari, Cittadella Universitaria, S.P.8–km 0.700, 09042 Monserrato, Cagliari, Italy.

**KEYWORDS:** *Pseudomonas*, bacterial porins, sugar transport, molecular dynamics, metadynamics, Trojan horse approach.

**ABSTRACT:** Deciphering the transport through outer-membrane porins is crucial to understand how antinfectives enter Gram-negative bacteria and perform their function. Here we elucidated the transport mechanism of substrates through the Pseudomonads sugar-specific porin OprB by means of multiscale modeling. We used molecular dynamics simulations to quantify the energetics of transport and thus a diffusion model to quantify the macroscopic flux of molecules through OprB. Our results show that Trp171 and several glutamate residues in the constriction region are key for transport of glucose, the preferred natural substrate, through OprB. The unveiled transport mechanism suggests that 2-acetamido-1,2-dideoxynojirimycin (DNJ-NAc), an antinfective structurally similar to glucose, can enter the cell via OprB. We quantified its energetics and macroscopic flux through OprB providing a comparative analysis with the natural substrate. Thus this pore can be considered a promising gateway for exploiting the Trojan-horse strategy in pathogen bacteria.

## INTRODUCTION

The antibiotic-resistance crisis has become a major public health problem, especially for Gram negative bacteria.<sup>1</sup> These are included in the World Health Organization 2017 list of ‘priority-1’ pathogens as well as in the antibiotic-resistant list of ESKAPE pathogens,<sup>2</sup> as they cause dangerous hospital-acquired infections. The case of Gram-negative pathogens is critical as the presence of the additional outer membrane (OM) imposes a physical barrier for the penetration of any molecule. Having an appropriate antibacterial activity on the target pathogen is not enough to have an efficient drug.<sup>3</sup> Thus, understanding the molecular mechanism of drug transport through the OM is an essential and very challenging step in drug discovery.<sup>4</sup>

Due to the hydrophobicity of the OM, the main gateway for polar antibiotics to enter the cell are porins.<sup>5,6</sup> Opportunistic pathogens such as *Pseudomonas aeruginosa* and *Acinetobacter Baumannii* express only specific porins to uptake different nutrients,<sup>7</sup> and the absence of general porins as in Enterobacteriaceae dramatically decreases permeability across the OM.<sup>8</sup> To overcome this issue, siderophore receptors have been proposed as potential gateway within the so-called Trojan Horse strategy:<sup>9-11</sup> molecules able to bind iron and structurally similar to natural substrates can be transported inside bacteria and act as a vector/cargo of antibacterial activity.<sup>12,13</sup>

However, siderophore receptors<sup>14</sup> undergo conformational changes during transport and require energy to function, with a limitation on the transport rate. Here we propose and demonstrate the same Trojan Horse strategy considering only specific channels functioning on passive transport, not requiring energetically-driven large conformational changes for transport of molecules. Specifically, we have investigated OprB, a substrate-specific porin located at the outer membrane that is responsible for the carbohydrate uptake in pseudomonads. A high-resolution X-ray structure of OprB from *Pseudomonas Putida* is available,<sup>15</sup> and the homologous porin from *P. aeruginosa* (*PaOprB*) has 80% sequence identity, with the main residues of the constriction region conserved. Therefore, the obtained results are transferable to the opportunistic pathogen.

The *in vitro* and *in vivo* characterization of this porin showed its preference for neutral monosaccharides (glucose being preferred), and a very low permeability for saccharides of more than one sugar unit.<sup>15-18</sup> It was also observed that the channel allows the transport of small non-sugar molecules such as lysine or arginine; and that glutamic acid and glucuronate (a carboxylated monosaccharide) cannot pass through, since the constriction region (CR) is negatively charged.<sup>15</sup> Previous structural studies of OprB<sup>15</sup> showed that this outer membrane protein is a monomer of  $\approx 30$  kDa which exhibits a 16 stranded  $\beta$ -barrel, where L2 and L3 loops (residues 81-116 and 136-175, respectively) fold inwards the pore shaping the CR (Figure 1). The L3 loop has a conserved disulfide bond (Cys148-Cys156). The L2 loop is long and is not involved, as in other porins, to the stabilization of the trimeric structure. In fact, the maltoporin LamB from *Escherichia coli*, another well-known carbohydrate-specific porin, exists as a trimer instead. LamB prefers larger carbohydrates because of the presence of a row of aromatic residues that lines the channel, highlighting the importance of van der Waals interactions in sugar recognition.<sup>19,20</sup> Meanwhile, OprB lacks this hydrophobic character, since only has two Trp residues along the channel (Trp108 and Trp171). However, polar residues are present in both eyelet regions to interact with the hydroxyl groups of carbohydrates, indicating that hydrogen bond interactions are also important in sugar transport.

Here we investigated the transport mechanism of glucose by OprB employing all-atom molecular dynamics simulations. Unveiling its features for transport, we showed how a positively charged NagZ inhibitor, DNJ-NAc (2-acetamido-1,2-dideoxynojirimycin),<sup>21</sup> structurally similar to glucose, follows the same mechanism of transport. In order to fight against pathogenic organisms, several approaches are being followed, such as inhibiting the biofilm formation in chronic infections, or the development of new inhibitors in combination with known antibiotics.<sup>22</sup> In the latter case, NagZ inhibition has gained interest, since this enzyme is involved in the very first step of the bacterial cell-wall recycling and regulates gene expression of the  $\beta$ -lactam resistance enzyme,  $\beta$ -lactamase.<sup>23,24</sup> Hence, the inhibitors that target this enzyme are claimed to be good candidates to act in synergy with  $\beta$ -lactam antibiotics and, consequently, the development of NagZ inhibitors is an active field of research.<sup>21,25,26</sup>

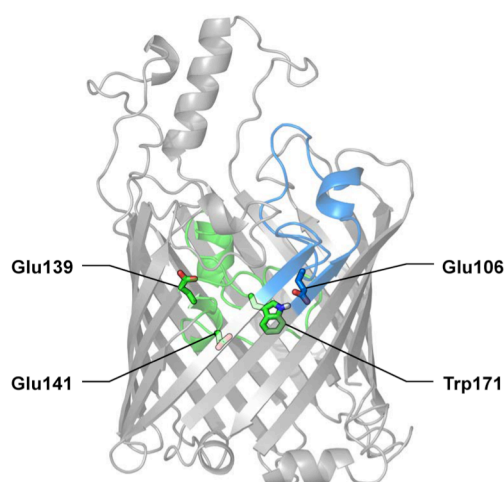


**Figure 1.** OprB structure. L2 and L3 loops are shown in blue and green, respectively.

## COMPUTATIONAL METHODS

The initial structure of OprB from *Pseudomonas putida* was taken from the high-resolution X-ray crystal structure of OprB (PDB entry 4GEY).<sup>15</sup> Though the OM is in fact an asymmetric bilayer composed by LPS on the external leaflet, very recent results showed that the transport of substrates through specific porins is mainly modulated by the interior of the pore, not the LPS region.<sup>27</sup> Thus we modeled our system as the protein embedded in a bilayer composed of 200 pre-equilibrated POPC phospholipid molecules using the CHARMM-GUI Membrane Builder.<sup>28</sup> The channel of the porin was centered and aligned considering the vector between Lys9 and Arg110 as a Z axis (positive Z values as the extracellular side; and negative Z values as the periplasmic side). After that, methionine mutations were reverted (i.e., Leu220Met and Val222Met), and the disulfide bridge between Cys148 and Cys156 was specified. The system was solvated with a TIP3P water box, together with 42 K<sup>+</sup> and 32 Cl<sup>-</sup> ions to neutralize the total charge of the system and reach a physiological KCl concentration of 150 mM, leading to a total of 61373 atoms (Figure S1). This same buffer was used in the experimental characterization of OprB.<sup>16</sup> Amber ff14SB<sup>29</sup>, TIP3P<sup>30</sup>, GAFFlipid<sup>31</sup> and GLYCAM<sup>32</sup> forcefields were used for the protein, water, the POPC bilayer and glucose, respectively. The DNJ-NAc inhibitor was parametrized using the antechamber module,<sup>33</sup> altogether with GAFF<sup>34</sup> parameters and the atomic charges obtained from first principles calculations using Gaussian09<sup>35</sup> at the HF/6-31G\* level of theory. The protonation state of all residues was assigned at neutral pH, and histidine residues were protonated according their chemical environment. All simulations were performed in periodic boundary conditions employing the ACEMD program<sup>36</sup>, a molecular dynamics engine running on GPU. ACEMD, as other MD packages, allows setting a time step of 4 fs by using hydrogen mass repartitioning.<sup>37</sup> This method does alter the kinetics of fastest stretching modes (N-H, O-H and C-H) without affecting kinetics and thermodynamics, thus allowing a more efficient sampling.<sup>38</sup> Therefore, the time step was set to 4 fs with the hydrogen mass scaled to 4 uma. The long-range contribution to the electrostatic potential was calculated employing the particle mesh Ewald (PME) method and using the optimal parameters in ACEMD set for a cutoff value of 9 Å.<sup>36</sup>

The OprB porin was equilibrated at 300 K during 4 ns in the NPT ensemble (Berendsen barostat) during several steps (see details in SI). Then, 100 ns were enough to equilibrate OprB in the NVT ensemble (Langevin thermostat), considering a cell dimension of 77.75 × 77.75 × 102.17 Å<sup>3</sup> (Figures S2-S3). Subsequently, a

production run of 1  $\mu$ s was performed. The  $\beta$ -barrel structure confers high stability to these proteins, which we monitored through the calculation of the protein RMSD, stable at 1.5 Å during all the simulation (Figure S5).

The lipid bilayer was analyzed employing the GridMAT-MD software.<sup>39</sup> From 100 frames obtained along the 1  $\mu$ s trajectory, the top and bottom membrane layers exhibit an average area per lipid of  $62.21 \pm 0.94$  Å<sup>2</sup> and  $60.97 \pm 1.79$  Å<sup>2</sup>, respectively. These results are lower than the experimental data (65 to 68 Å<sup>2</sup>).<sup>40</sup> However, projecting the average area per lipid onto the average x-y position for each lipid head (Figure S1), we observe how the regions surrounding the protein exhibit a lower area per lipid, due to the fact that the interaction of the lipids with the hydrophobic belt of the protein is stronger than the lipid-lipid interaction. In the intermediate regions the average area per lipid is comparable to the experimental one (for a lipid only membrane) hence, the protein is not affected by its periodic image. The external region exhibits some artifacts (very low area per lipid) due to the fact that in the area per lipid analysis we are neglecting periodic boundary conditions.

From the production run, we calculated the main physical descriptors of OprB for permeability.<sup>41</sup> Starting from the equilibrated structure we investigated the transport mechanism of glucose and DNJ-NAC through this porin by means of the enhanced sampling technique metadynamics.<sup>42</sup> Two geometrical collective variables (CVs) were defined (see scheme in SI), as already used in the past to investigate the transport of molecules through porins.<sup>43</sup> The first CV (CV<sub>1</sub>) is the Z component of the distance between the center of mass of the substrate (heavy atoms only) and the center of mass of C<sub>α</sub> atoms of the  $\beta$ -barrel of the porin. The second CV (CV<sub>2</sub>) was defined as the Z component of the radius vector between atoms C2 and C3 of the substrate. While the former allows following the position of the substrate along the axis of diffusion Z, the latter explores the orientational conformations of the substrate inside the pore.<sup>44</sup> Multiple-walkers<sup>45</sup> and well-tempered<sup>46</sup> approaches were used in order to accelerate the sampling and obtain a converged free energy surface (FES). The height of the Gaussian terms was set at 1 kcal/mol, its widths were set at 0.30 and 0.10 Å for CV<sub>1</sub> and CV<sub>2</sub>, respectively. A Gaussian function was deposited every 10 ps of simulation. The temperature was set at 300 K and the bias factor at 10. Multiple-walkers metadynamics simulations were run until convergence was reached (see SI).

## RESULTS AND DISCUSSION

The main physical descriptors for permeability (Figure 2) were analyzed from a 1  $\mu$ s production run. The average radius of the pore at the CR is quite small ( $\approx 2$  Å, Figure 2a and 2b), similar to that of other specific porins like OprE<sup>8</sup> ( $\approx 1.77$  Å) and OccAB<sup>47</sup> ( $\approx 2$  Å) indicating that only small molecules can pass through, as is evidenced by experiments.<sup>15</sup>

The distribution of charge along the Z axis has been computed on the X-ray

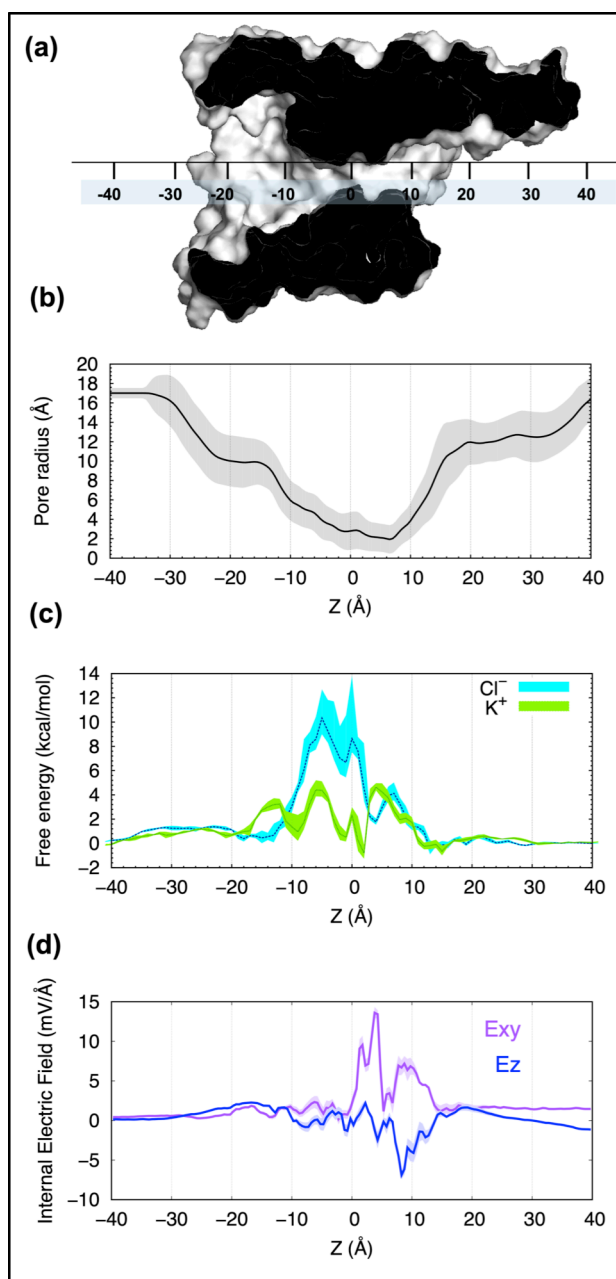


**Figure 2.** OprB characterization. (a) Cut-through of OprB surface, showing the interior of the channel. (b) Pore radius along the Z axis of the pore. (c) FE diagram for Cl<sup>-</sup> and K<sup>+</sup> ion diffusion (blue and green, respectively). (d) Transversal (blue) and longitudinal (magenta) electric field along the diffusion axis Z of the pore. Shaded areas correspond to the standard deviation.

structure considering the point charges assigned to each atom by the force field (see Figure S7). The CR is negatively charged and a preference for cations is seen from the free energy profile calculated for potassium and chloride ions inside the OprB pore (Figure 2c). This calculation was obtained starting from the production run analyzing both K<sup>+</sup> and Cl<sup>-</sup> ion densities from 4 replica of 200 ns at 1M concentration

of KCl. As expected, the free energy (FE) barrier for anions ( $\text{Cl}^-$  ions) in the CR is bigger ( $\approx 10$  kcal/mol) than that of cations ( $\text{K}^+$  ions,  $\approx 4$  kcal/mol). This is in good agreement with the experimentally observed OprB transport preferences for neutral/positive compounds.<sup>15</sup>

Similar to other specific and non-specific porins<sup>8,41,48,49</sup> the highest intensity of the internal electric field<sup>50</sup> is located in the CR in the transverse direction (XY) to the axis of diffusion (Z) (Figure 2d). The strength is comparable to that of the general porin OmpC from *Escherichia Coli*.<sup>41</sup> The longitudinal component (Z) is negative above the CR and almost zero in the CR and periplasmic region (Figure 2d). This implies that positive molecules once in the extracellular vestibule are pulled toward the CR.

After having characterized the intrinsic properties of OprB (Figure 2), we aimed to understand the transport mechanism of its preferred substrate glucose. We employed metadynamics with the two geometrical CVs described in the computational methods section. The simulations lasted  $1.74 \mu\text{s}$  (4 walkers of 435 ns each, see SI) and the obtained results are shown in Figure 3a.

The global minimum of the projected one-dimensional FE profile (Figure 4a) is located at  $Z \approx 0 \text{ \AA}$  (channel center) and acts as a binding site. This minimum corresponds in the two-dimensional FES to minima 2 and 3 (Figure 3a), which are symmetrical since despite the 180 degrees inversion of glucose, the interactions are conserved: one hydrogen bond with Glu139 and two with Glu141, while the hydroxymethyl group interacts with Glu106. Additionally, Trp171 establishes a carbohydrate-aromatic stacking with the pyranose ring of glucose, since all its C-H bonds are axially oriented and can establish CH/ $\pi$  contacts with an aromatic system. It is worth to mention that Glu106 is always well-oriented to interact with glucose since maintains a salt bridge with Arg83, and therefore their sidechains are rigid.

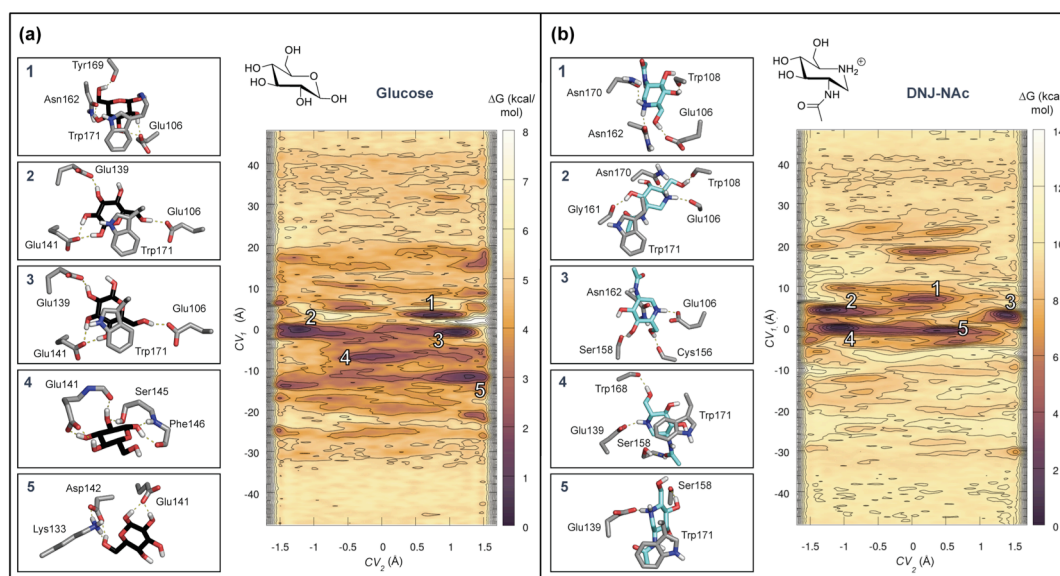


**Figure 3.** Metadynamics of the transport mechanism through OprB of (a) glucose and (b) DNJ-NAC. For each molecule, the chemical structure of each substrate and the obtained two-dimensional FES ( $\text{CV}_1$  and  $\text{CV}_2$ ), where the more relevant minima have been analyzed. Representative structures of each minimum are shown in panels 1-5. Carbon atoms are colored in gray, black and cyan in order to distinguish OprB, glucose and DNJ-NAC, respectively. Isolines are set at 1 kcal/mol.

Before reaching the global minimum, glucose is stabilized at  $Z \approx 3 \text{ \AA}$  by interacting only with Glu106, the sidechain of Asn162 and the carbonyl group of the backbone of Tyr169 (minimum 1, 0.5 kcal/mol higher in energy than minima 2 and 3). Once the

barrier from the global minimum is crossed (negative values of  $Z$ ), the hydrogen bond with Glu141 is conserved and further stabilized by other interactions with Ser145 and the carbonyl group of the backbone of Phe146 (minimum 4), or Asp142 and Lys133 (minimum 5). These minima are respectively 1.5 and 0.7 kcal/mol higher in energy than the global minimum. From the latter, two free energy barriers can be identified from the one-dimensional FE profile: 2.6 and 3.8 kcal/mol depending on if the substrate enters (negative  $Z$  values) or exits (positive  $Z$  values) the channel, respectively. Therefore, once the binding site is reached, is easier to enter inside the periplasmic space rather than exiting.

Thus, glucose permeation is mediated by two main type of interactions. On one side, a stacking interaction provided by Trp171, and on the other side, hydrogen bonds with glutamate residues in the CR (Glu139 and Glu141, negatively charged; and Glu106 neutralized by Arg83) provide the negatively charged character of this part of the channel, preventing the passage of negative molecules. Considering the molecular structure of glucose, with all its hydroxyl groups in an equatorial configuration, it is not surprising that several conformations play a role in the permeation mechanism. These results are in good agreement with the transport preferences observed in experiments<sup>15</sup> (not negatively charged monosaccharides) and bring light to the main transport features of OprB. Moreover, in the X-ray crystal of glucose complexed with OprB,<sup>15</sup> also a hydroxyl group from the substrate interacts with Glu106. The other hydroxyl groups interact with the backbone carbonyl groups of Glu106, Trp108, Asn170 and Trp171. Surprisingly, Trp171 do not establish a stacking with glucose. However, the precise position and orientation of the substrate cannot be inferred from the X-ray structure since there is still considerable ambiguity with regard to the glucose electron density. This might be due to the conformational diversity that glucose exhibits in the center of the pore, which may be difficult to capture by crystallographic techniques.

In view of the observed properties of the OprB channel, we have studied the transport of DNJ-NAc, an iminosugar that inhibits the NagZ enzyme. DNJ-NAc is a positively charged carbohydrate-based compound, and thus it would be able to establish a carbohydrate-stacking with Trp171, hydrogen bonds with Glu106 and ionic interactions with Glu139 and Glu141. Moreover, the conformational space of DNJ-NAc is probably limited in comparison with glucose, since the ammonium and *N*-acetamido groups are located at the positions of the ring oxygen (O5) and C2 of a typical pyranose ring, respectively, leading to a highly asymmetric molecule. Thus, it is not clear whether the passage of DNJ-NAc through OprB can take place with a specific molecular orientation and, more specifically, whether the voluminous *N*-acetamido group can pass through the small CR.

The metadynamics simulation of DNJ-NAc permeability (Figure 3b) lasted 2.24  $\mu$ s (4 walkers of 560 ns each) and it was performed using a similar computational setup as the one specified for glucose. The one-dimensional profile (figure 4a) exhibits a global minimum at  $Z = 0$  Å (minima 4 and 5 in the two-dimensional FES), as it was the case for glucose. As DNJ-NAc starts to penetrate inside the pore ( $Z \approx 7$  Å), its ammonium group interacts with the carbonyl groups of Asn162 and Asn170 sidechains, while the hydroxymethyl group interacts with Glu106 (minimum 1, 2.9 kcal/mol higher in energy than the global minimum). While the substrate approaches the pore center, we can observe two minima at 4 and 3 Å (minima 2 and 3, respectively). In the former, DNJ-NAc establishes hydrogen bonds with the Asn170 sidechain and the backbone carbonyl groups of Glu106, Trp108 and Gly161. In addition, a CH/ $\pi$  interaction between the methyl group of the *N*-acetamido group and Trp171 further stabilizes this pose. In the latter minimum, the ammonium group establishes a salt bridge with Glu106, while the DNJ-NAc hydroxyl groups interact with Cys156 and Ser158 backbones by hydrogen bonding. In the OprB center ( $Z = 0$  Å, global minimum in the one-dimensional FE profile), we identified two binding poses (minima 4 and 5, in the two-dimensional FES). Both exhibit an ionic interaction between the carboxylate sidechain of Glu139 and the ammonium group of DNJ-NAc, and one hydrogen bond between a hydroxyl group of the substrate and a carbonyl

group of the protein backbone. Nevertheless, the interaction with Trp171 differs: while in minimum 4 we found a stacking with the pyranose ring, in minimum 5 the *N*-acetamido group of DNJ-NAc establishes a CH/ $\pi$  interaction. Minimum 4 is about 2 kcal/mol more stable than minimum 5, probably because of the *N*-acetamido group is also stabilized by a hydrogen bond with Ser158. Moreover, hydroxyl groups at positions C3 and C4 are oriented towards the sidechain of Glu106, despite having water molecules between them; this might further stabilize this configuration.

In summary, DNJ-NAc is oriented inside OprB such that it forms a salt bridge with Glu139 and interacts with Trp171 either by CH/ $\pi$  interaction or stacking. Surprisingly, the size of the *N*-acetamido substituent is not a problem at all to pass the CR. In fact, the methyl group provides additional CH/ $\pi$  interactions with the aromatic system of Trp171, and ultimately helps to maintain the desired orientation. Interestingly, the one-dimensional FE profiles show a clear preference for both substrates to bind near the central region (see Figure 4a). This preference is more marked for the positively charged DNJ-NAc, reminiscent of the selectivity of OprB for cations. The presence of a central affinity region is in contrast with general porins that exhibit instead a marked central steric barrier.<sup>41</sup> Nevertheless, since OprB is selective for neutral/positive monosaccharides, we do observe a high energy barrier ( $\approx 20$  kcal/mol) when we analyzed the transport through OprB of glucuronate, a negatively charged monosaccharide that is structurally similar to glucose, only differing in the presence of a carboxylate group in position 6 instead of the hydroxymethyl (Figure S11).

Additional simulations were performed to quantify the macroscopic transport properties by imposing a gradient concentration of both glucose and DNJ-NAc substrates from *cis* to *trans*. We combined the one-dimensional diffusion model with the two-state Markov model, as described in detail in SI. The flux of molecules for different gradient concentrations is shown in Figure 4b. The flux is similar up to a micromolar gradient concentration, with a slight preference for the DNJ-NAc molecule. However, by increasing the gradient, the positive DNJ-NAc shows saturation due to the deep affinity for OprB at the constriction region. On the other hand, the neutral glucose saturates above the millimolar concentration. In the case of specific channels, the strength of affinity is a parameter to check for optimizing transport in the range of expected/physiological concentration gradient.<sup>51</sup>

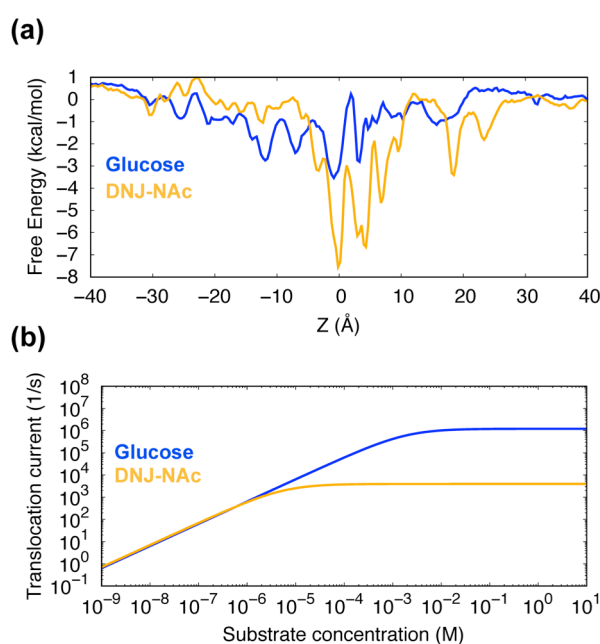


**Figure 4.** Molecular flux over the free energy surface of OprB. (a). Free energy projection onto the axis of diffusion for glucose and DNJ-NAc. (b) Calculated flux through OprB for different concentrations of glucose (red) and DNJ-NAc (green).

## CONCLUSIONS

By using multiscale modeling, we have explored the intrinsic permeation properties of OprB, rationalizing the transport preferences of this specific-porin at atomistic level, both for the transport of glucose (natural substrate) and the glucose mimic DNJ-NAc as potential antinfective. Residues located at the CR (Glu106, Glu139, Glu141 and Trp171) control the transport through OprB, screening both the charge and the size of molecules. These results led us to propose the class of specific porins as potential candidates for transporting antibacterial compounds using a Trojan Horse approach, once their natural substrates are known. Further chemical modifications of DNJ-NAc might lead to improve its capabilities.

Specifically, examining the obtained binding poses for DNJ-NAc, positions C4 or C5 of the “pyranose ring” are aligned with the Z axis of the pore, and thus may be proper positions to attach a linker in order to use DNJ-NAc as a vector to introduce other antimicrobial molecules inside Pseudomonads. However, other modifications such as introducing a hydroxymethyl group in position C3 or C4 instead of position C5 would decrease the transport since having a direct hydrogen bond interaction with the carboxylate group of Glu106, as occurs with glucose (Figure 3a, panels 2 and 3), are expected to stabilize even more the binding.

The advantages to use specific porins as Trojan Horse entrance is their passive mode of transport, which do not require energy and/or large conformational changes and thus allow higher rates of transport. Eventually, this is an example of the use of computational methods and in particular multiscale modelling for rational design of drugs with enhanced transport. Combining the calculations of the potential of mean force with the 1D diffusion model we were able to move from the mechanism of transport to the quantification of the macroscopic flux of substrates through OprB.

## ASSOCIATED CONTENT

### Supporting Information

Computational details, equilibration and production analysis (RMSD and RMSF), point charge calculations along the Z axis of the pore, metadynamics convergence analysis, and calculation of the macroscopic flux are available in the supplementary file.

## AUTHOR INFORMATION

### Corresponding Author

\*E-mail: [matteo.ceccarelli@dsf.unica.it](mailto:matteo.ceccarelli@dsf.unica.it).

### Present Addresses

SAG present address: Department of Chemistry, University College London, London, UK.

## ABBREVIATIONS

CR, constriction region; FES, free energy surface; CV, collective variable; DNJ-NAc, 2-acetamido-1,2-dideoxynojirimycin.

## ACKNOWLEDGMENT

The research leading to these results was conducted as part of the “Translocation” consortium ([www.translocation.com](http://www.translocation.com)) and has received support from the Innovative Medicines Initiatives Joint Undertaking under Grant Agreement no. 115525, resources that are composed of financial contribution from the European Union’s seventh framework programme (FP7/2007-2013) and EFPIA companies in kind contribution.

This work was also supported by MINECO (CTQ2017-85496-P), AGAUR (2017SGR-1189) and the Spanish Structures of Excellence María de Maeztu (MDM-

2017-0767).

J. C. acknowledges MINECO for a predoctoral fellowship (FPI-BES-2015-072055). MC would like to thank the support of MIUR with the PRIN project 2015795S5W\_005.

## REFERENCES

- 1 E. Tacconelli, N. Magrini, Y. Carmeli, S. Harbarth, G. Kahlmeter, J. Kluytmans, M. Mendelson, C. Pulcini, N. Singh and U. Theuretzbacher, *World Health Organization*, 2017, 1–7.
- 2 R. Tommasi, D. G. Brown, G. K. Walkup, J. I. Manchester and A. A. Miller, *Nat. Rev. Drug Discov.*, 2015, **14**, 529–542.
- 3 D. G. Brown, T. L. May-Dracka, M. M. Gagnon and R. Tommasi, *J. Med. Chem.*, 2014, **57**, 10144–10161.
- 4 R. Tommasi, R. Iyer and A. A. Miller, *ACS Infect. Dis.*, 2018, **4**, 686–695.
- 5 J. M. Pagès, C. E. James and M. Winterhalter, *Nat. Rev. Microbiol.*, 2008, **6**, 893–903.
- 6 M. A. Scorciapino, S. Acosta-Gutierrez, D. Benkerrou, T. D’Agostino, G. Mallocci, S. Samanta, I. Bodrenko and M. Ceccarelli, *J. Phys. Condens. Matter*, 2017, **29**, 113001.
- 7 S. Chevalier, E. Bouffartigues, J. Bodilis, O. Maillot, O. Lesouhaitier, M. G. J. Feuilloley, N. Orange, A. Dufour and P. Cornelis, *FEMS Microbiol. Rev.*, 2017, **41**, 698–722.
- 8 S. Samanta, I. Bodrenko, S. Acosta-Gutierrez, T. D’Agostino, M. Pathania, I. Ghai, C. Schleberger, D. Bumann, R. Wagner, M. Winterhalter, B. Van Den Berg and M. Ceccarelli, *ACS Infect. Dis.*, 2018, **4**, 1519–1528.
- 9 A. Luscher, P. Saint Auguste, D. Bumann, L. Mazza, J. H. Naismith and D. Pletzer, *Antimicrob. Agents Chemother.*, 2018, **62**, 1–11.
- 10 G. S. Tillotson, *Infect. Dis. Res. Treat.*, 2016, **9**, 45–52.
- 11 I. J. Schalk, *J. Med. Chem.*, 2018, **61**, 3842–3844.
- 12 M. A. Scorciapino, G. Mallocci, I. Serra, S. Milenkovic, L. Moynié, J. H. Naismith, E. Desarbre, M. G. P. Page and M. Ceccarelli, *BioMetals*, 2019, **32**, 155–170.
- 13 L. Moynié, I. Serra, M. A. Scorciapino, E. Oueis, M. G. Page, M. Ceccarelli and J. H. Naismith, *Elife*, 2018, e42270.
- 14 J. D. Faraldo-Gómez and M. S. P. Sansom, *Nat. Rev. Mol. Cell Biol.*, 2003, **4**, 105–116.
- 15 B. Van Den Berg, *J. Biol. Chem.*, 2012, **287**, 41044–41052.
- 16 E. G. Saravolac, N. F. Taylor, R. Benz and R. E. W. Hancock, *J. Bacteriol.*, 1991, **173**, 4970–4976.
- 17 J. L. Wylie and E. A. Worobec, *J. Bacteriol.*, 1995, **177**, 3021–3026.
- 18 L. O. Adewoye, L. Tschetter, J. O’Neil and E. A. Worobec, *J. Bioenerg. Biomembr.*, 1998, **30**, 257–267.
- 19 T. Schirmer, T. A. Keller, Y. Wang and J. P. Rosenbusch, *Science (80-. )*, 1995, **267**, 512–514.
- 20 R. Dutzler, Y. F. Wang, P. J. Rizkallah, J. P. Rosenbusch and T. Schirmer, *Structure*, 1996, **4**, 127–134.
- 21 T. Yamaguchi, B. Blázquez, D. Heseck, M. Lee, L. I. Llarrull, B. Boggess, A. G. Oliver, J. F. Fisher and S. Mobashery, *ACS Med. Chem. Lett.*, 2012, **3**, 238–242.
- 22 S. Wagner, R. Sommer, S. Hinsberger, C. Lu, R. W. Hartmann, M. Empting and A. Titz, *J. Med. Chem.*, 2016, **59**, 5929–5969.
- 23 I. Acebrón, K. V. Mahasenan, S. De Benedetti, M. Lee, C. Artola-Recolons, D. Heseck, H. Wang, J. A. Hermoso and S. Mobashery, *J. Am. Chem. Soc.*, 2017, **139**, 6795–6798.
- 24 D. A. Dik, J. F. Fisher and S. Mobashery, *Chem. Rev.*, 2018, **118**, 5952–5984.
- 25 K. A. Stubbs, M. Balcewich, B. L. Mark and D. J. Vocadlo, *J. Biol. Chem.*, 2007, **282**, 21382–21391.
- 26 L. A. Ho, J. L. Winogrodzki, A. W. Debowski, Z. Madden, D. J. Vocadlo, B. L. Mark and K. A. Stubbs, *Chem. Commun.*, 2018, **54**, 10630–10633.
- 27 F. Samsudin and S. Khalid, *J. Phys. Chem. B*, 2019, DOI: 10.1021/acs.jpcc.9b00063.
- 28 E. L. Wu, X. Cheng, S. Jo, H. Rui, K. C. Song, E. M. Dávila-Contreras, Y. Qi, J. Lee, V. Monje-Galvan, R. M. Venable, J. B. Klauda and W. Im, *J. Comput. Chem.*, 2014, **35**, 1997–2004.
- 29 J. A. Maier, C. Martinez, K. Kasavajhala, L. Wickstrom, K. E. Hauser and C. Simmerling, *J. Chem. Theory Comput.*, 2015, **11**, 3696–3713.

- 30 W. L. Jorgensen, J. Chandrasekhar, J. D. Madura, R. W. Impey and M. L. Klein, *J. Chem. Phys.*, 1983, **79**, 926.
- 31 C. J. Dickson, L. Rosso, R. M. Betz, R. C. Walker and I. R. Gould, *Soft Matter*, 2012, **8**, 9617–9627.
- 32 K. N. Kirschner, A. Yongye, S. Tschampel M., J. González-Outeiriño, C. R. Daniels, B. L. Foley and R. J. Woods, *J. Comput. Chem.*, 2008, **29**, 622–655.
- 33 J. Wang, W. Wang, P. A. Kollman and D. A. Case, *J. Mol. Graph. Model.*, 2006, **25**, 247–260.
- 34 J. M. Wang, R. M. Wolf, J. W. Caldwell, P. a Kollman and D. a Case, *J. Comput. Chem.*, 2004, **25**, 1157–1174.
- 35 G. M. J. Frisch, G. W. Trucks, H. B. Schlegel, G. E. Scuseria, M. A. Robb, J. R. Cheeseman, A. Scalmani, V. Barone, B. Mennucci, G. A. Petersson, H. Nakatsuji, M. Caricato, X. Li, H. P. Hratchian, J. F. Izmaylov, J. Bloino, G. Zheng, J. L. Sonnenberg, M. Hada, M. Ehara, K. Toyota, R. Fukuda, J. E. Hasegawa, M. Ishida, T. Nakajima, Y. Honda, O. Kitao, H. Nakai, T. Vreven, J. A. Montgomery, Jr., J. Peralta, F. Ogliaro, M. Bearpark, J. J. Heyd, E. Brothers, K. N. Kudin, V. N. Staroverov, R. Kobayashi, J. M. Normand, K. Raghavachari, A. Rendell, J. C. Burant, S. S. Iyengar, J. Tomasi, M. Cossi, N. Rega, R. E. Millam, M. Klene, J. E. Knox, J. B. Cross, V. Bakken, C. Adamo, J. Jaramillo, R. Gomperts, K. M. Stratmann, O. Yazyev, A. J. Austin, R. Cammi, C. Pomelli, J. W. Ochterski, R. L. Martin, J. B. V. G. Zakrzewski, G. A. Voth, P. Salvador, J. J. Dannenberg, S. Dapprich, A. D. Daniels, O. Farkas and and D. J. F. Foresman, J. V. Ortiz, J. Cioslowski, .
- 36 M. J. Harvey, G. Giupponi and G. De Fabritiis, *J. Chem. Theory Comput.*, 2009, **5**, 1632–1639.
- 37 K. A. Feenstra, B. Hess and H. J. C. Berendsen, *J. Comput. Chem.*, 1999, **20**, 786–798.
- 38 C. W. Hopkins, S. Le Grand, R. C. Walker and A. E. Roitberg, *J. Chem. Theory Comput.*, 2015, **11**, 1864–1874.
- 39 D. R. B. William J. Allen, Justin A. Lemkul, *J. Comput. Chem.*, 2009, **30**, 1952–1958.
- 40 N. Kučerka, M. P. Nieh and J. Katsaras, *Biochim. Biophys. Acta - Biomembr.*, 2011, **1808**, 2761–2771.
- 41 S. Acosta-Gutierrez, L. Ferrara, M. Pathania, M. Masi, J. Wang, I. Bodrenko, M. Zahn, M. Winterhalter, R. A. Stavenger, J. M. Pages, J. H. Naismith, B. Van Den Berg, M. Page and M. Ceccarelli, *ACS Infect. Dis.*, 2018, **4**, 1487–1498.
- 42 A. Laio and M. Parrinello, *Proc. Natl. Acad. Sci. U. S. A.*, 2002, **99**, 12562–12566.
- 43 S. Acosta-Gutierrez, M. A. Scorciapino, I. Bodrenko and M. Ceccarelli, *J. Phys. Chem. Lett.*, 2015, **6**, 1807–1812.
- 44 H. Bajaj, S. Acosta Gutierrez, I. Bodrenko, G. Mallocci, M. A. Scorciapino, M. Winterhalter and M. Ceccarelli, *ACS Nano*, 2017, **11**, 5465–5473.
- 45 P. Raiteri, A. Laio, F. L. Gervasio, C. Micheletti and M. Parrinello, *J. Phys. Chem. B*, 2006, **110**, 3533–3539.
- 46 A. Barducci, G. Bussi and M. Parrinello, *Phys. Rev. Lett.*, 2008, **100**, 1–4.
- 47 D. Benkerrou and M. Ceccarelli, *Phys. Chem. Chem. Phys.*, 2018, **20**, 8533–8546.
- 48 M. Pathania, S. Acosta-Gutierrez, S. P. Bhamidimarri, A. Baslé, M. Winterhalter, M. Ceccarelli and B. van den Berg, *Structure*, 2018, **26**, 708–721.
- 49 L. G. M. Ferrara, G. D. Wallat, L. Moynié, N. N. Dhanasekar, S. Aliouane, S. Acosta-Gutiérrez, J. M. Pagès, J. M. Bolla, M. Winterhalter, M. Ceccarelli and J. H. Naismith, *J. Mol. Biol.*, 2016, **428**, 4528–4543.
- 50 S. Acosta-Gutiérrez, I. Bodrenko, M. A. Scorciapino and M. Ceccarelli, *Phys. Chem. Chem. Phys.*, 2016, **18**, 8855–8864.
- 51 A. M. Berezhkovskii and S. M. Bezrukov, *Biophys. J.*, 2005, **88**, L17–L19.